



Very Compact Millimeter Sizes for Composite Star-forming/AGN Submillimeter Galaxies

Soh Ikarashi¹, Karina I Caputi¹, Kouji Ohta², R. J. Ivison^{3,4}, Claudia D. P Lagos⁵, Laura Bisigello^{1,6}, Bunyo Hatsukade⁷, Itziar Aretxaga⁸, James S Dunlop³, David H Hughes⁸, Daisuke Iono^{9,10}, Takuma Izumi¹¹, Nobunari Kashikawa^{10,11}, Yusei Koyama^{9,10,12}, Ryohei Kawabe^{9,10}, Kotaro Kohno^{7,13}, Kentaro Motohara⁷, Kouichiro Nakanishi^{9,10}, Yoichi Tamura¹⁴, Hideki Umehata¹⁵, Grant W Wilson¹⁶, Kiyoto Yabe¹⁷, and Min S Yun¹⁶

¹ Kapteyn Astronomical Institute, University of Groningen, P.O. Box 800, 9700 AV Groningen, The Netherlands; sikarash@astro.rug.nl

² Department of Astronomy, Kyoto University, Kitashirakawa-Oiwake-Cho, Sakyo-ku, Kyoto 606-8502, Japan

³ Institute for Astronomy, University of Edinburgh, Royal Observatory, Blackford Hill, Edinburgh EH9 3HJ, UK

⁴ European Southern Observatory, Karl Schwarzschild Str. 2, D-85748 Garching, Germany

⁵ International Centre for Radio Astronomy Research, University of Western Australia, 7 Fairway, Crawley 6009, Perth WA, Australia

⁶ SRON Space Research of Netherlands, 9747 AD, Groningen, The Netherlands

⁷ Institute of Astronomy, University of Tokyo, 2-21-1 Osawa, Mitaka, Tokyo 181-0015, Japan

⁸ Instituto Nacional de Astrofísica, Óptica y Electrónica (INAOE), Aptdo. Postal 51 y 216, 72000 Puebla, Mexico

⁹ National Astronomical Observatory, Mitaka, Tokyo 181-8588, Japan

¹⁰ SOKENDAI (The Graduate University for Advanced Studies), Shonan Village, Hayama, Kanagawa 240-0193, Japan

¹¹ Optical and Infrared Astronomy Division, National Astronomical Observatory, Mitaka, Tokyo 181-8588, Japan

¹² Subaru Telescope, 650 North A'ohoku Place, Hilo, HI 96720, USA

¹³ Research Center for the Early Universe, School of Science, University of Tokyo, 7-3-1 Hongo, Bunkyo, Tokyo 113-0033, Japan

¹⁴ Institute for Advanced Research, Nagoya University, Furo-cho, Chikusa-ku, Nagoya 464-8601, Japan

¹⁵ The Open University of Japan, 2-11 Wakaba, Mihama-ku, Chiba 261-8586, Japan

¹⁶ Department of Astronomy, University of Massachusetts, Amherst, MA 01003, USA

¹⁷ Kavli Institute for the Physics and Mathematics of the Universe (WPI), The University of Tokyo, 5-1-5 Kashiwanoha, Kashiwa, Chiba 277-8583, Japan

Received 2017 June 29; revised 2017 October 20; accepted 2017 October 23; published 2017 November 9

Abstract

We report the study of the far-infrared (IR) sizes of submillimeter galaxies (SMGs) in relation to their dust-obscured star formation rate (SFR) and active galactic nuclei (AGN) presence, determined using mid-IR photometry. We determined the millimeter-wave ($\lambda_{\text{obs}} = 1100 \mu\text{m}$) sizes of 69 Atacama Large Millimeter/submillimeter Array (ALMA)-identified SMGs, selected with $\geq 10\sigma$ confidence on ALMA images ($F_{1100 \mu\text{m}} = 1.7\text{--}7.4 \text{ mJy}$). We found that all of the SMGs are located above an avoidance region in the size-flux plane, as expected by the Eddington limit for star formation. In order to understand what drives the different millimeter-wave sizes in SMGs, we investigated the relation between millimeter-wave size and AGN fraction for 25 of our SMGs at $z = 1\text{--}3$. We found that the SMGs for which the mid-IR emission is dominated by star formation or AGN have extended millimeter-sizes, with respective median $R_{\text{c,e}} = 1.6^{+0.34}_{-0.21}$ and $1.5^{+0.93}_{-0.24}$ kpc. Instead, the SMGs for which the mid-IR emission corresponds to star-forming/AGN composites have more compact millimeter-wave sizes, with median $R_{\text{c,e}} = 1.0^{+0.20}_{-0.20}$ kpc. The relation between millimeter-wave size and AGN fraction suggests that this size may be related to the evolutionary stage of the SMG. The very compact sizes for composite star-forming/AGN systems could be explained by supermassive black holes growing rapidly during the SMG coalescing, star-formation phase.

Key words: galaxies: evolution – galaxies: formation – galaxies: high-redshift – submillimeter: galaxies

1. Introduction

The morphology and size of star-forming regions in submillimeter galaxies (SMGs) are important properties with which we can address the nature of their prodigious, dust-obscured star formation, and consequently the formation and evolution of the most massive galaxies. The Atacama Large Millimeter/submillimeter Array (ALMA) is enabling astronomers to image high-redshift SMGs with angular resolutions of $\lesssim 0.^{\prime\prime}3$. Some ALMA studies have reported effective radii (R_{e}) of $\sim 0.3\text{--}3$ kpc (e.g., Ikarashi et al. 2015; Simpson et al. 2015; Hodge et al. 2016). These radii are small compared with what astronomers expected from studies of SMG sizes based on radio continuum and CO emission (e.g., Tacconi et al. 2006; Biggs & Ivison 2008; Ivison et al. 2011). These new results represent a new milestone in our understanding of star formation in SMGs, suggesting that these galaxies plausibly

evolve to compact quiescent galaxies (e.g., Toft et al. 2014; Ikarashi et al. 2015; Simpson et al. 2015).

As a next step, it would be useful to test the hypothesis that SMGs are connected to the formation of the most massive galaxies, being triggered by major mergers, and then evolving into compact quiescent galaxies via quenching in a quasi-stellar object (QSO) phase (e.g., Sanders et al. 1988; Hopkins et al. 2008; Toft et al. 2014). The compact submillimeter sizes of SMGs, including recent reports of the existence of subkiloparsec-scale starburst cores (Iono et al. 2016; Ikarashi et al. 2017; Oteo et al. 2017), suggests that the intense star-formation activity might be quenched by active galactic nuclei (AGN), as observed in some luminous QSOs (e.g., Maiolino et al. 2012; Carniani et al. 2016). However, previous X-ray (e.g., Alexander et al. 2005; Wang et al. 2013) and mid-infrared (IR; e.g., Ivison et al. 2004; Coppin et al. 2010; Serjeant et al. 2010) studies indicate that some SMGs do harbor AGN.

In this Letter, we report a millimeter-wave size study of 69 ALMA-identified AzTEC SMGs. Firstly, we study the empirical relation between ALMA continuum flux densities and the millimeter-wave sizes of SMGs. Secondly, we investigate the relationship between millimeter-wave sizes and the presence of AGN in SMGs at $z = 1\text{--}3$, as determined from mid-IR data.

We adopt throughout a cosmology with $H_0 = 70 \text{ km s}^{-1} \text{ Mpc}^{-1}$, $\Omega_M = 0.3$, and $\Omega_\Lambda = 0.7$.

2. ALMA Observations and Samples

The sample used in this paper comes from our ALMA 1100 μm continuum imaging survey of 144 bright AzTEC/ASTE sources with $F_{1100 \mu\text{m}, \text{AzTEC}} \geq 2.4 \text{ mJy}$ in the Subaru/*XMM-Newton* Deep Field (SXDF; Furusawa et al. 2008). The SXDF survey was conducted in the ALMA Cycles 2 and 3 (2013.1.00781, 2015.1.00442.S; PI: Hatsukade; B. Hatsukade et al. 2017, in preparation).

The ALMA observations in Cycle 2 were carried out with the array configurations C34-5 and C34-7, with 37–38 working 12-m antennas covering up to a *uv* distance of $\sim 1500 \text{ k}\lambda$. In Cycle 3, the observations were executed in array configuration C40-4, covering up to a *uv* distance of $\sim 1000 \text{ k}\lambda$. On-source integration times per source in each cycle were 0.6 min. The typical synthesized beam size for our ALMA continuum images is $\sim 0''.30 \times 0''.23$ ($\text{PA} \sim 56^\circ$), after combining the Cycle 2 and 3 data. The average rms noise level is $120 \mu\text{Jy beam}^{-1}$. The images were generated with Briggs weighting, using a robust parameter of 0.3.

The ALMA continuum maps yielded 70 ALMA-identified AzTEC SMGs (hereafter ASXDF SMGs) with $S_{\text{peak}}/N \geq 10$ detections, suitable for reliable ALMA millimeter-wave size measurements (e.g., Ikarashi et al. 2015). We removed one lensed SMG (ASXDF1100.001; Ikarashi et al. 2011), leaving 69 SMGs. ALMA fluxes were remeasured in tapered ALMA images with a synthesized beam of $\sim 0''.6$, which is larger than the measured mm-wave sizes of SMGs in this paper, using the IMFIT task in CASA.

For 51 ASXDF SMGs, we obtained well-constrained photometric redshifts, with a median error $\delta z = 0.13 \pm 0.02$, based on the individual $1-\sigma$ errors estimated by *Le Phare* (e.g., Ilbert et al. 2006) in spectral energy distribution (SED) model fitting using the B , V , R_C , i' , z' , J , H , K_S , 3.6, and 4.5 μm data (S. Ikarashi et al. 2017, in preparation). The remaining SMGs lie outside the coverage of the optical/near-IR images, or have individual $1-\sigma$ errors of >1 . Photometric and spectroscopic redshifts from the literature are listed in Table 1.

3. ALMA Millimeter-wave Source Size Measurements

We measured millimeter-wave sizes as circularized effective radii ($R_{\text{c.e.}}$) for the 69 ASXDF SMGs with ALMA visibility data, in the same manner as Ikarashi et al. (2015). We used *uv* distance versus amplitude plots (hereafter *uv*-amp plots) for our measurements. Although the ALMA data cover *uv* distances up to $\sim 1500 \text{ k}\lambda$, we used only data at $\leq 500 \text{ k}\lambda$, which corresponds to a scale of $\sim 0''.2$. Adopting this cutoff for the longest *uv* distance is the equivalent of smoothing with a larger size kernel in the image plain. We aim to mitigate the effects of possible clumpy structures in the size measurements and to measure $R_{\text{c.e.}}$ robustly. For the sources detected with $\geq 10\sigma$ in the ALMA Cycle-2 images alone, we measured their sizes

using only Cycle-2 data, to avoid effects due to any systematic absolute flux calibration offsets between our Cycle 2 and 3 data.¹⁸ We measured sizes by fitting a Gaussian model to the observed data in the *uv*-amp plots. When we measure the size, the other sources ($\geq 5\sigma$) in each ALMA image were removed from the visibility data based on simple source properties derived by the IMFIT task.

In order to estimate possible systematics in the size measurements, we injected mock sources into ALMA noise visibility images, generated from the actual ALMA data as in Ikarashi et al. (2015). Briefly we injected a symmetric Gaussian component for a range of source sizes and flux densities that cover the putative parameter range of our ASXDF sources with uniform probability. As tested in Ikarashi et al. (2015), our method can measure circularized effective radii correctly even if a source has an asymmetric Gaussian profile. We corrected our raw measured sizes based on the results of the simulations for the data used in this paper.

As a result, we obtained ALMA millimeter-wave sizes of $0''.08\text{--}0''.68$ (FWHM) for the 69 ASXDF SMGs. Note that ASXDF1100.009.1 has two distinct millimeter-wave components with a separation of $\sim 0''.6$, sharing a host galaxy at $z_{\text{spec}} = 0.9$.

4. Relation Between Millimeter Sizes and Fluxes

Figure 1 (left panel) shows all 69 ASXDF SMGs in an ALMA 1100- μm versus millimeter-wave size plot. Additionally, we plot 13 ALMA-identified, fainter SMGs at $z \gtrsim 3$ from Ikarashi et al. (2015). ASXDF SMGs are absent from the top-left and the bottom-right corners of this plot. The expected source selection limit for $\geq 10\sigma$ continuum detection based on simple Gaussian models explains the absence of SMGs in the top-left corner. The bottom-right corner, instead, is free from any such selection biases, so the absence of SMGs requires an explanation.

The absence of SMGs in the bottom-right corner of Figure 1 can be interpreted as the influence of Eddington-limited star formation (Murray et al. 2005). According to Younger et al. (2008), which reported pioneering studies of maximum star formation in bright SMGs, a maximum star-formation rate is given by

$$\text{SFR}_{\text{max}} = 480\sigma_{400}^2 D_{\text{kpc}} \kappa_{100}^{-1} M_{\odot} \text{yr}^{-1}, \quad (1)$$

where D_{kpc} is the characteristic physical scale of the starburst region in kpc, σ_{400} is the line-of-sight gas velocity dispersion in units of 400 km s^{-1} , and κ_{100} is the dust opacity in units of $100 \text{ cm}^2 \text{ g}^{-1}$. Here we adopt a Chabrier initial mass function (Chabrier 2003), $\kappa_{100} = 1$, as in Younger et al. (2008), and a median gas velocity dispersion of 510 km s^{-1} from CO line observations of SCUBA SMGs (Bothwell et al. 2013). We also adopt $2 \times \text{FWHM}$ or $4 \times R_{\text{c.e.}}$, which is expected to include 94% of a total light, as D_{kpc} . The derived SFR_{max} was corrected with this factor of 0.94.

In order to plot the relation between SFR and physical scale described by Equation (1) on Figure 1 (the left panel), we assume a fixed redshift $z = 2$. The conversion factors from ALMA fluxes to SFRs were derived by bootstrapping given a

¹⁸ Comparisons of the fluxes of ASXDF sources in our Cycle-1, 2, and 3 data indicated that the fluxes in the Cycle-3 data are systematically $\sim 20\%$ smaller. Therefore, we corrected the primary flux calibration for this effect.

Table 1
Summary Data of the ASXDF SMG Samples Used in this Paper

ID	R.A. (J2000)	Decl. (J2000)	SNR	$F_{100\mu\text{m}}$ (mJy)	z_{photo}	SFR ($M_{\odot}\text{ yr}^{-1}$)	mm-wave Size (FWHM; arcsec)	mm-wave Size ($R_{\text{c},\epsilon}; \text{kpc}$)	AGN (mid-IR)
ASXDF1100.002.1	2:17:30.63	-4:59:36.8	15	4.81 ± 0.43	$3.3^{+0.07}_{-0.87}$	990^{+720}_{-340}	$0.42^{+0.06}_{-0.02}$	$1.6^{+0.2}_{-0.1}$...
ASXDF1100.004.1	2:18:05.65	-5:10:49.7	14	4.39 ± 0.56	$3.5^{+0.35}_{-0.16}$	880^{+420}_{-290}	$0.40^{+0.06}_{-0.04}$	$1.5^{+0.2}_{-0.1}$...
ASXDF1100.005.1	2:17:30.45	-5:19:22.5	25	7.24 ± 0.45	$0.7^{+0.01}_{-0.01}$	1200^{+990}_{-420}	$0.34^{+0.04}_{-0.02}$	$1.2^{+0.1}_{-0.1}$...
ASXDF1100.006.1	2:17:27.32	-5:06:42.8	10	5.11 ± 0.50	$4.5^{+0.18}_{-0.15}$	930^{+340}_{-330}	$0.68^{+0.06}_{-0.06}$	$2.2^{+0.2}_{-0.2}$...
ASXDF1100.007.1	2:18:03.01	-5:28:42.0	20	6.26 ± 0.53	$3.2^{+0.28}_{-0.22}$	1300^{+930}_{-450}	$0.32^{+0.04}_{-0.02}$	$1.2^{+0.1}_{-0.1}$...
ASXDF1100.008.1	2:16:47.93	-5:01:29.9	12	6.45 ± 0.59	$2.2^{+0.02}_{-0.08}$	1500^{+950}_{-460}	$0.62^{+0.06}_{-0.06}$	$2.6^{+0.2}_{-0.2}$	AGN
ASXDF1100.009.1A	2:17:42.11	-4:56:27.6	19	4.68 ± 0.40	(0.5) ^a	550^{+430}_{-190}	$0.30^{+0.02}_{-0.04}$	$0.9^{+0.1}_{-0.1}$...
ASXDF1100.009.1B	2:17:42.16	-4:56:28.5	11	1.16 ± 0.12	(0.5) ^a	140^{+110}_{-50}	$0.10^{+0.08}_{-0.06}$	$0.6^{+0.5}_{-0.4}$...
ASXDF1100.011.1	2:17:50.59	-5:30:59.2	13	4.22 ± 0.41	$5.5^{+0.08}_{-0.63}$	730^{+440}_{-260}	$0.38^{+0.04}_{-0.04}$	$1.1^{+0.1}_{-0.1}$...
ASXDF1100.014.1 [†]	2:17:29.77	-5:03:18.6	11	3.12 ± 0.17	$2.2^{+0.04}_{-0.03}$	690^{+270}_{-210}	$0.50^{+0.06}_{-0.08}$	$2.1^{+0.2}_{-0.3}$	SF
ASXDF1100.016.1	2:16:41.11	-5:03:51.4	19	4.79 ± 0.35	$5.0^{+0.54}_{-0.06}$	850^{+390}_{-240}	$0.24^{+0.02}_{-0.04}$	$0.8^{+0.1}_{-0.1}$...
ASXDF1100.018.1	2:18:13.83	-4:57:43.5	14	3.47 ± 0.32	$1.7^{+0.09}_{-0.02}$	850^{+650}_{-280}	$0.26^{+0.04}_{-0.04}$	$1.1^{+0.2}_{-0.2}$	NO
ASXDF1100.020.1*	2:18:23.73	-5:11:38.5	13	4.94 ± 0.43	$2.7^{+0.01}_{-0.01}$	1100^{+460}_{-380}	$0.30^{+0.04}_{-0.02}$	$1.2^{+0.2}_{-0.1}$...
ASXDF1100.021.1	2:18:16.49	-4:55:08.8	16	4.03 ± 0.28	$2.3^{+0.03}_{-0.04}$	920^{+720}_{-310}	$0.28^{+0.02}_{-0.04}$	$1.1^{+0.1}_{-0.2}$	COM
ASXDF1100.022.1	2:18:42.68	-4:59:32.1	15	3.09 ± 0.31	$2.3^{+0.01}_{-0.06}$	710^{+550}_{-240}	$0.20^{+0.04}_{-0.04}$	$0.8^{+0.2}_{-0.2}$	COM
ASXDF1100.023.2	2:18:20.40	-5:31:43.2	10	2.17 ± 0.27	$2.5^{+0.10}_{-0.12}$	480^{+350}_{-160}	$0.16^{+0.10}_{-0.06}$	$0.6^{+0.4}_{-0.2}$...
ASXDF1100.025.2 [†]	2:17:32.59	-4:50:26.4	13	2.34 ± 0.12	$3.4^{+0.16}_{-0.07}$	470^{+320}_{-150}	$0.34^{+0.06}_{-0.04}$	$1.3^{+0.2}_{-0.1}$...
ASXDF1100.029.1 [†]	2:17:20.80	-4:49:49.5	11	2.67 ± 0.21	$2.8^{+0.16}_{-0.17}$	570^{+360}_{-180}	$0.46^{+0.08}_{-0.10}$	$1.8^{+0.3}_{-0.4}$	AGN
ASXDF1100.031.1 [†]	2:17:37.24	-4:47:53.0	13	2.09 ± 0.15	$2.5^{+0.18}_{-0.12}$	480^{+380}_{-170}	$0.28^{+0.04}_{-0.06}$	$1.1^{+0.2}_{-0.2}$	COM
ASXDF1100.033.1	2:18:03.56	-4:55:27.3	15	4.86 ± 0.33	(2.6) ^b	1100^{+860}_{-350}	$0.34^{+0.04}_{-0.02}$	$1.4^{+0.2}_{-0.1}$	COM
ASXDF1100.034.1	2:17:59.32	-5:05:04.6	11	2.84 ± 0.32	(1.6) ^c	680^{+640}_{-220}	$0.16^{+0.08}_{-0.06}$	$0.7^{+0.3}_{-0.3}$...
ASXDF1100.035.1 ^{†,*}	2:17:35.37	-5:28:37.3	12	2.09 ± 0.12	$2.7^{+0.07}_{-0.11}$	450^{+360}_{-150}	$0.52^{+0.08}_{-0.08}$	$2.1^{+0.3}_{-0.3}$...
ASXDF1100.041.1	2:17:53.87	-5:26:35.7	10	2.91 ± 0.29	$0.8^{+0.09}_{-0.00}$	520^{+260}_{-180}	$0.42^{+0.06}_{-0.10}$	$1.6^{+0.2}_{-0.4}$...
ASXDF1100.042.1	2:18:38.29	-5:03:18.3	12	3.26 ± 0.40	$3.2^{+0.02}_{-0.01}$	680^{+440}_{-240}	$0.42^{+0.04}_{-0.06}$	$1.6^{+0.1}_{-0.2}$...
ASXDF1100.044.1	2:17:45.85	-5:00:56.7	12	1.93 ± 0.26	$6.8^{+0.20}_{-0.72}$	330^{+210}_{-84}	$0.09^{+0.07}_{-0.05}$	$0.2^{+0.2}_{-0.1}$...
ASXDF1100.046.1	2:17:13.34	-4:58:57.4	16	4.00 ± 0.32	$3.5^{+0.01}_{-0.10}$	810^{+620}_{-280}	$0.28^{+0.04}_{-0.04}$	$1.0^{+0.1}_{-0.1}$...
ASXDF1100.047.1 [†]	2:17:56.73	-4:52:39.0	11	2.25 ± 0.17	$2.2^{+0.01}_{-0.02}$	500^{+400}_{-160}	$0.40^{+0.08}_{-0.06}$	$1.6^{+0.3}_{-0.2}$	SF
ASXDF1100.048.1 [†]	2:17:46.16	-4:47:47.2	14	2.55 ± 0.11	$2.5^{+0.21}_{-0.12}$	570^{+460}_{-200}	$0.40^{+0.06}_{-0.04}$	$1.6^{+0.2}_{-0.2}$	NO
ASXDF1100.050.1*	2:18:22.30	-5:07:37.0	11	3.32 ± 0.40	$3.0^{+0.15}_{-0.15}$	700^{+360}_{-240}	$0.24^{+0.08}_{-0.08}$	$0.9^{+0.3}_{-0.3}$...
ASXDF1100.051.1 [†]	2:18:23.96	-5:32:07.8	12	2.63 ± 0.23	$0.7^{+0.00}_{-0.04}$	430^{+270}_{-150}	$0.08^{+0.06}_{-0.04}$	$0.3^{+0.2}_{-0.1}$...
ASXDF1100.051.2 [†]	2:18:24.59	-5:31:48.5	11	2.88 ± 0.23	$4.7^{+0.24}_{-0.15}$	520^{+270}_{-160}	$0.30^{+0.10}_{-0.06}$	$1.0^{+0.3}_{-0.2}$...
ASXDF1100.052.1 [†]	2:17:33.17	-5:01:54.5	11	2.05 ± 0.14	$2.8^{+0.25}_{-0.65}$	440^{+340}_{-150}	$0.34^{+0.04}_{-0.06}$	$1.3^{+0.2}_{-0.2}$	AGN
ASXDF1100.055.1 [†]	2:17:20.03	-5:13:05.8	13	2.54 ± 0.15	$2.1^{+0.02}_{-0.24}$	570^{+290}_{-180}	$0.34^{+0.06}_{-0.06}$	$1.4^{+0.2}_{-0.2}$	SF
ASXDF1100.057.1	2:17:32.41	-5:12:50.9	12	3.54 ± 0.38	$1.9^{+0.04}_{-0.11}$	820^{+360}_{-260}	$0.34^{+0.04}_{-0.06}$	$1.4^{+0.2}_{-0.3}$	AGN
ASXDF1100.076.1	2:16:41.04	-5:01:12.5	13	4.13 ± 0.55	$4.8^{+0.13}_{-0.41}$	750^{+550}_{-230}	$0.34^{+0.04}_{-0.06}$	$1.1^{+0.1}_{-0.2}$...
ASXDF1100.077.1 [†]	2:18:11.00	-4:49:51.9	12	1.69 ± 0.20	$4.1^{+0.02}_{-0.12}$	320^{+190}_{-110}	$0.22^{+0.08}_{-0.08}$	$0.8^{+0.3}_{-0.3}$...
ASXDF1100.089.1	2:18:10.64	-5:34:53.6	21	4.73 ± 0.30	$5.4^{+0.11}_{-0.09}$	830^{+600}_{-200}	$0.24^{+0.04}_{-0.02}$	$0.7^{+0.1}_{-0.1}$...
ASXDF1100.095.1 [†]	2:17:12.97	-5:14:12.2	10	1.91 ± 0.19	$2.2^{+0.11}_{-0.08}$	440^{+320}_{-150}	$0.32^{+0.08}_{-0.08}$	$1.3^{+0.3}_{-0.3}$	AGN
ASXDF1100.100.1	2:17:53.25	-4:49:51.5	13	2.84 ± 0.29	$2.2^{+0.16}_{-0.08}$	670^{+460}_{-210}	$0.24^{+0.04}_{-0.04}$	$1.0^{+0.2}_{-0.2}$	COM
ASXDF1100.105.1	2:18:02.86	-5:00:31.6	13	2.86 ± 0.30	(1.1) ^c	630^{+460}_{-220}	$0.24^{+0.06}_{-0.08}$	$1.0^{+0.2}_{-0.3}$	COM
ASXDF1100.107.1 [†]	2:18:07.85	-5:25:49.3	11	1.67 ± 0.16	$4.6^{+0.18}_{-0.86}$	310^{+190}_{-80}	$0.34^{+0.06}_{-0.06}$	$1.1^{+0.2}_{-0.2}$...
ASXDF1100.115.1	2:16:59.42	-5:10:55.8	12	4.23 ± 0.33	(0.6) ^a	600^{+500}_{-220}	$0.50^{+0.06}_{-0.06}$	$1.7^{+0.2}_{-0.2}$...
ASXDF1100.134.1	2:17:54.80	-5:23:23.8	15	3.27 ± 0.27	$2.5^{+0.16}_{-0.05}$	740^{+500}_{-260}	$0.24^{+0.06}_{-0.04}$	$1.0^{+0.2}_{-0.2}$	COM
ASXDF1100.156.1	2:16:38.33	-5:01:21.5	11	3.33 ± 0.31	$1.8^{+0.04}_{-0.10}$	810^{+630}_{-260}	$0.34^{+0.06}_{-0.06}$	$1.4^{+0.3}_{-0.3}$	SF
ASXDF1100.188.1 ^{†,*}	2:16:41.94	-5:07:04.3	10	2.42 ± 0.18	$2.6^{+0.28}_{-0.20}$	530^{+450}_{-180}	$0.22^{+0.10}_{-0.08}$	$0.9^{+0.4}_{-0.3}$...
ASXDF1100.203.1 [†]	2:18:23.15	-5:27:02.0	11	1.90 ± 0.12	$2.5^{+0.03}_{-0.15}$	440^{+330}_{-150}	$0.34^{+0.10}_{-0.10}$	$1.4^{+0.4}_{-0.4}$	NO
ASXDF1100.227.1	2:17:44.27	-5:20:08.6	24	7.42 ± 0.57	$3.7^{+0.35}_{-0.14}$	1400^{+760}_{-510}	$0.34^{+0.02}_{-0.02}$	$1.2^{+0.1}_{-0.1}$...
ASXDF1100.228.1	2:18:09.66	-5:18:43.1	12	3.11 ± 0.34	$1.9^{+0.05}_{-0.10}$	740^{+610}_{-240}	$0.38^{+0.06}_{-0.06}$	$1.6^{+0.3}_{-0.2}$	SF
ASXDF1100.229.1	2:18:18.84	-4:50:29.9	11	3.60 ± 0.36	$2.3^{+0.05}_{-0.11}$	820^{+620}_{-270}	$0.26^{+0.06}_{-0.08}$	$1.1^{+0.2}_{-0.3}$	COM
ASXDF1100.235.1	2:17:36.00	-5:20:34.4	13	4.64 ± 0.40	$2.3^{+0.04}_{-0.14}$	1100^{+820}_{-370}	$0.26^{+0.06}_{-0.04}$	$1.1^{+0.2}_{-0.2}$	COM
ASXDF1100.236.1 [†]	2:17:21.54	-5:19:07.7	11	1.65 ± 0.14	$2.4^{+0.02}_{-0.02}$	370^{+250}_{-120}	$0.15^{+0.09}_{-0.09}$	$0.6^{+0.4}_{-0.4}$	COM
ASXDF1100.247.1 [†]	2:16:33.85	-5:02:42.7	11	1.87 ± 0.18	$2.6^{+0.11}_{-0.14}$	410^{+260}_{-140}	$0.24^{+0.08}_{-0.10}$	$1.0^{+0.3}_{-0.4}$	COM
ASXDF1100.003.1 [†]	2:16:44.48	-5:02:21.6	15	2.85 ± 0.13	$0.36^{+0.04}_{-0.04}$
ASXDF1100.010.1	2:17:39.79	-5:29:19.2	24	5.94 ± 0.37	$0.28^{+0.02}_{-0.02}$
ASXDF1100.026.1 [†]	2:17:42.55	-5:29:00.3	11	1.69 ± 0.17	$0.18^{+0.06}_{-0.12}$
ASXDF1100.040.1	2:17:55.24	-5:06:45.1	15	3.14 ± 0.35	$0.20^{+0.06}_{-0.04}$
ASXDF1100.053.1	2:16:48.20	-4:58:59.6	10	4.02 ± 0.51	$0.42^{+0.06}_{-0.06}$

Table 1
(Continued)

ID	R.A. (J2000)	Decl. (J2000)	SNR	$F_{1100\mu\text{m}}$ (mJy)	z_{photo}	SFR ($M_{\odot}\text{ yr}^{-1}$)	mm-wave Size (FWHM; arcsec)	mm-wave Size ($R_{\text{c,e}}$; kpc)	AGN (mid-IR)
ASXDF1100.054.1	2:17:15.41	-4:57:55.6	11	4.12 ± 0.38	$0.38^{+0.06}_{-0.06}$
ASXDF1100.068.1	2:17:42.17	-5:25:46.8	12	3.24 ± 0.30	$0.24^{+0.04}_{-0.06}$
ASXDF1100.070.1 [†]	2:18:46.15	-5:04:12.5	12	2.17 ± 0.13	$0.30^{+0.04}_{-0.06}$
ASXDF1100.074.1	2:18:33.31	-4:58:07.0	10	2.77 ± 0.33	$0.32^{+0.06}_{-0.06}$
ASXDF1100.097.1	2:18:18.54	-5:34:34.7	11	2.53 ± 0.26	$0.20^{+0.08}_{-0.06}$
ASXDF1100.097.2 [†]	2:18:17.61	-5:34:27.9	10	2.14 ± 0.26	$0.32^{+0.08}_{-0.10}$
ASXDF1100.133.1	2:18:05.51	-5:35:46.5	11	2.25 ± 0.26	$0.08^{+0.08}_{-0.04}$
ASXDF1100.161.1 [†]	2:18:13.76	-5:37:27.3	12	2.68 ± 0.20	$0.44^{+0.06}_{-0.06}$
ASXDF1100.168.1	2:18:04.37	-5:34:03.5	11	1.79 ± 0.21	$0.16^{+0.08}_{-0.06}$
ASXDF1100.213.1 [†]	2:18:44.02	-5:35:31.3	12	2.90 ± 0.28	$0.16^{+0.08}_{-0.08}$
ASXDF1100.231.1	2:17:59.65	-4:46:49.8	12	2.88 ± 0.36	$0.28^{+0.08}_{-0.08}$
ASXDF1100.243.1 [†]	2:16:50.43	-5:10:16.2	10	2.09 ± 0.20	$0.37^{+0.09}_{-0.11}$
ASXDF1100.252.1	2:17:05.65	-5:15:04.9	12	2.62 ± 0.25	$0.24^{+0.06}_{-0.08}$

Notes. [†] ALMA flux, SNR, and size measurements are conducted in the ALMA data after combining the Cycle 2 and 3 data. For sources without [†], all ALMA measurements were done in the ALMA Cycle-2 data. ^{*} The SMGs are not included in the analysis in Section 5 because of non-detection in 24 μm . [•] The SMGs are not included in the analysis in Section 5 because of source blending in the IRAC maps. See Section 5.1 for the columns of AGN.

^a Spectroscopic redshifts by cross-identification with the UDS-z survey catalog (e.g., Bradshaw et al. 2013; McLure et al. 2013).

^b Spectroscopic redshifts by cross-identification with the SCUBA SMGs (Coppin et al. 2010).

^c Spectroscopic redshifts by cross-identification with the SCUBA SMGs (Banerji et al. 2011).

dust temperature (T_{d}) distribution for lensed 1.3 mm-selected galaxies (Weiß et al. 2013) and an SED library with T_{d} information compiled in Swinbank et al. (2014). For these assumptions, we obtain a possible range for Eddington-limited star-formation rates.

For a more direct comparison of the millimeter fluxes and sizes of SMGs with Eddington-limited star formation, we replot 51 of the 69 SMGs at $z = 0.7$ –6.8 with optical/near-IR photometric or spectroscopic redshifts on the SFR–physical size plane (Figure 1, right panel). The SFRs are derived from $F_{1100\mu\text{m}}$, given the range of possible dust temperatures T_{d} and SEDs noted above. We assume that the AGN contribution to the submillimeter flux is negligible (see references in Rosario et al. 2012). In order to visualize the coverage of the size–SFR plane produced by the large SFR uncertainties (due to the unknown dust SED temperatures), we show the full SFR probability density distribution (rather than a single value) for each SMG. The results in both panels of Figure 1 show that the SMGs avoid the SFR region around the Eddington limit, suggesting that the minimum possible millimeter-wave sizes for bright SMGs are given by the Eddington limited star formation.

The empirical relation between flux and size can explain the discrepancy in the reported (sub)millimeter-wave (median) sizes of $0.^{\prime\prime}20^{+0.^{\prime\prime}03}_{-0.^{\prime\prime}05}$ by Ikarashi et al. (2015) and $0.^{\prime\prime}3 \pm 0.^{\prime\prime}04$ by Simpson et al. (2015). Given $F_{870\mu\text{m}}/F_{1100\mu\text{m}} = 2$ for conversion of the observed fluxes, Simpson et al. (2015) covered $F_{1100\mu\text{m}} \gtrsim 2.5$ mJy. In this regime, our ASXDF SMGs have a median size of $0.^{\prime\prime}31^{+0.^{\prime\prime}03}_{-0.^{\prime\prime}03}$.

5. Relation Between Millimeter Sizes and AGN

We present our studies of the connection between the millimeter-wave sizes and AGN in SMGs, based on a mid-IR AGN diagnostic. We consider 25 ALMA-identified SMGs with $1 < z_{\text{phot}} \text{ or } z_{\text{spec}} < 3$, which are detected in all IRAC and MIPS 24 μm images. All SMGs here have redshift information and a

single component at $\sim 0.^{\prime\prime}2$ resolution. More than 15 out of the 25 are located above $4\times$ the main sequence at $z \sim 2$ in the stellar mass versus SFR plane (Figure 2), indicating that the majority of the sample are starbursts (Bisigello et al. 2017). Note that among the 29 SMGs with $z = 1$ –3, four are not used in the analysis: two SMGs are not detected at 24 μm and the other are blended in the IRAC maps.

5.1. Mid-IR AGN Diagnostic

A 4.5 μm /8 μm /24 μm color-color plot has often been used as an AGN diagnostic for high-redshift, dusty infrared-luminous galaxies, such as SMGs and dusty-obscured galaxies (DOGs) at $z \sim 2$ (e.g., Ivison et al. 2004, 2007; Pope et al. 2008a, 2008b). We refer the reader to Kirkpatrick et al. (2015), who presented a detailed study of mid-IR SED evolution along AGN fraction for high- z galaxies. Empirical SED templates (top-left panel in Figure 3) suggest that high-redshift galaxies dominated by star formation or AGN in mid-IR light can be segregated from each other in the mid-IR color-color plane. The position of our 25 SMGs in this color-color plot shows that some of them do not follow either the model tracks for star-formation-dominated or AGN-dominated galaxies.

We generated the expected mid-IR colors of galaxies that are a composite of SF and AGN by combining SEDs of SF and AGN with various SF/AGN ratios. This “toy” color prediction reproduces the colors of “composite SMGs” which are likely to be dominated by neither an AGN nor a starburst in the mid-IR (top right panel in Figure 3).

We divided the 25 SMGs into four sub-groups based on their 4.5/8/24- μm colors: star-forming, composite, AGN-dominant, and “no class.” The criteria are:

1. $F_{8\mu\text{m}}/F_{4.5\mu\text{m}} < 1.15 \wedge F_{24\mu\text{m}}/F_{8\mu\text{m}} \geq 5$ (star-forming)
2. $F_{8\mu\text{m}}/F_{4.5\mu\text{m}} \geq 1.15 \wedge F_{24\mu\text{m}}/F_{8\mu\text{m}} \geq 5$ (composite)
3. $F_{8\mu\text{m}}/F_{4.5\mu\text{m}} \geq 1.50 \wedge F_{24\mu\text{m}}/F_{8\mu\text{m}} < 5$ (AGN)
4. $F_{8\mu\text{m}}/F_{4.5\mu\text{m}} < 1.50 \wedge F_{24\mu\text{m}}/F_{8\mu\text{m}} < 5$ (no class).

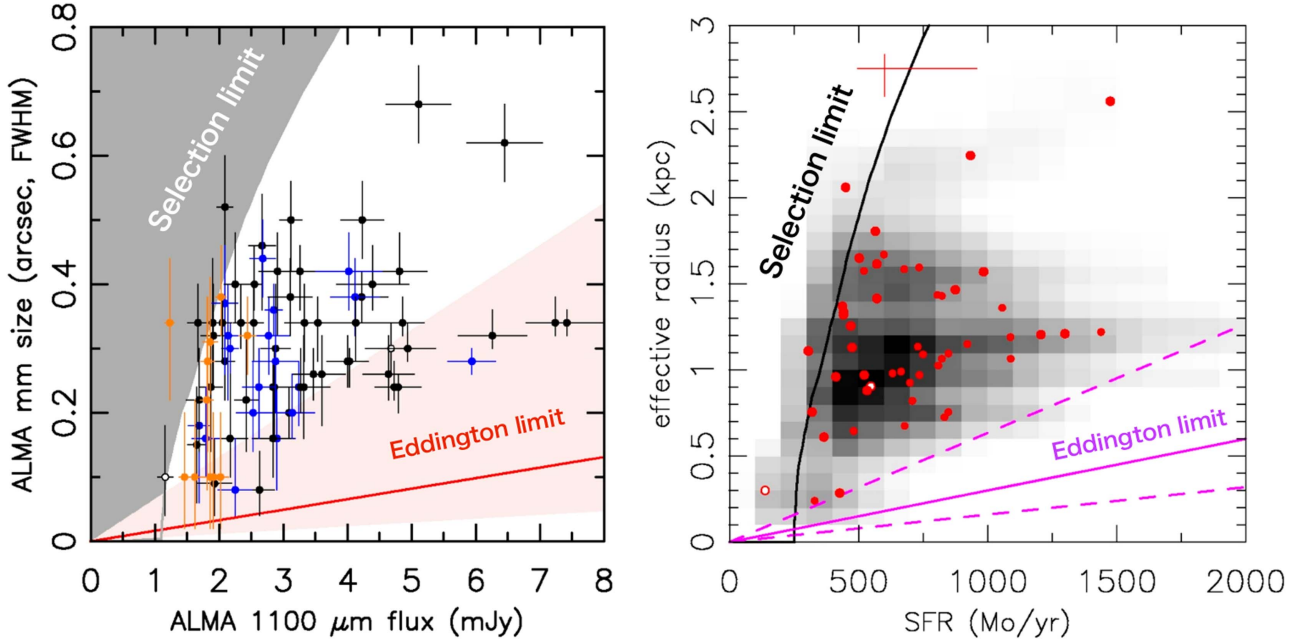


Figure 1. Left: ALMA 1100 μm vs. ALMA millimeter-wave size for the ASXDF SMGs with and without redshift information (filled black and blue circles, respectively). The black points correspond to the ASXDF SMGs obtained in our ALMA Cycle-2 and 3 projects, as analyzed in this paper. The gray shaded area shows the approximate selection limit (10σ) on our ALMA images. The orange points show other ASXDF SMGs at $z \gtrsim 3$ from Ikarashi et al. (2015). The light red shaded area shows a range of Eddington-limited star formation for the 1σ ranges of T_d and gas velocity dispersion of known SMGs from the literature. The red solid line shows Eddington-limited star formation for the medians of the T_d and gas velocity dispersion. Right: SFR vs. effective radii in physical scale for the 51 ASXDF SMGs with available photometric or spectroscopic redshifts. The selection limit assumes a physical scale for $z = 2$. The background gray shaded area shows $P(\text{SFR}, \text{size})$ for each SMG, taking into account the large uncertainty of the SFR due to the unknown dust temperature T_d . The Eddington-limit relation is marked with magenta lines (solid for the median and dashed for $\pm 1\sigma$ of the gas velocity dispersion). Typical error bars are indicated with a red cross in the upper part of the plot. Open circles in both panels mark ASXDF1100.009.1, which has two distinct components in the ALMA image.

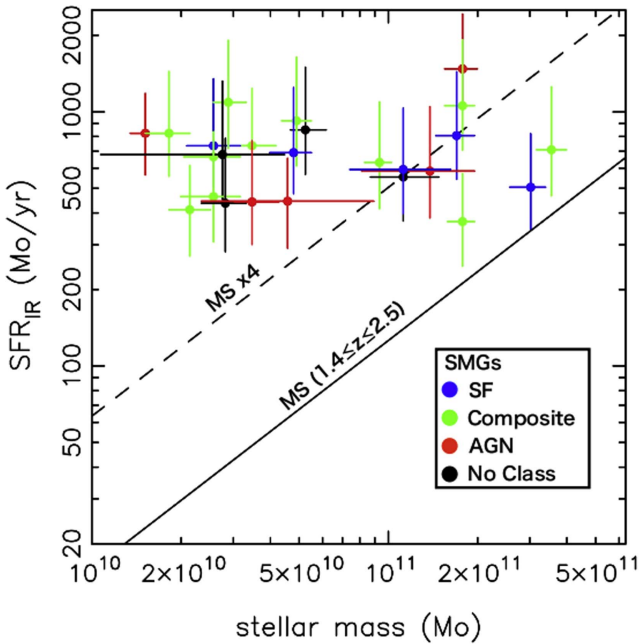


Figure 2. Stellar mass vs. SFR for the 25 ASXDF SMGs at $z \sim 1$ –3. The black solid line corresponds to the main sequence at $1.4 \leq z \leq 2.5$ (Daddi et al. 2007). Colors indicate the AGN classification based on IRAC/MIPS colors (see Section 5.1 and Figure 3 for details of this diagnostic).

The model colors (top, Figure 3) indicate that the SMGs categorized as “no class” could be in the star-forming or composite classes. Due to this ambiguity, we consider the “no class” separately.

Note that, in our diagnostic, the star-forming class and AGN-dominant class are defined first. We choose $F_{8 \mu\text{m}}/F_{4.5 \mu\text{m}} = 1.15$ as criteria for separation, as this ensures that all galaxies that satisfy neither an AGN criteria by Donley et al. (2012) nor another criteria by Stern et al. (2005) also lie on the star-forming region of the color-color diagram. The predicted 24 $\mu\text{m}/8 \mu\text{m}$ color evolution with redshift, as derived by public empirical mid-IR SED templates for high- z star-forming galaxies, composite galaxies, and AGN-dominant galaxies (Kirkpatrick et al. 2015), are shown with our sample SMGs (bottom left, Figure 3). For these templates, the respective mid-IR AGN fractions of each sample are <20, 20–80, $\geq 80\%$. In this plot we averaged the public SEDs in each AGN class, after scaling all fluxes at $\lambda_{\text{rest}} = 8 \mu\text{m}$. The predictions based on the Kirkpatrick et al. (2015) SED templates suggest that our criteria for 24 $\mu\text{m}/8 \mu\text{m}$ color can work to select AGN-dominant class, and show that our composite type is expected to have typically AGN fractions of around $\sim 50\%$, consistently with our “toy” models.

5.2. Results

In the millimeter-wave physical size versus SFR plot (bottom-right panel in Figure 3), all SMGs with composite mid-IR components are evidently more compact and located closer to the Eddington limit than the other SMGs with star-forming dominant or AGN-dominant mid-IR components.

The respective median $R_{\text{c,e}}$ for SMGs classified as star-forming dominant, composite, and AGN-dominant are $1.6^{+0.34}_{-0.21}$, $1.0^{+0.20}_{-0.20}$, and $1.5^{+0.93}_{-0.24}$ kpc. The size difference between the SMGs with composite and star-forming mid-IR components, and the difference between the SMGs with composite and

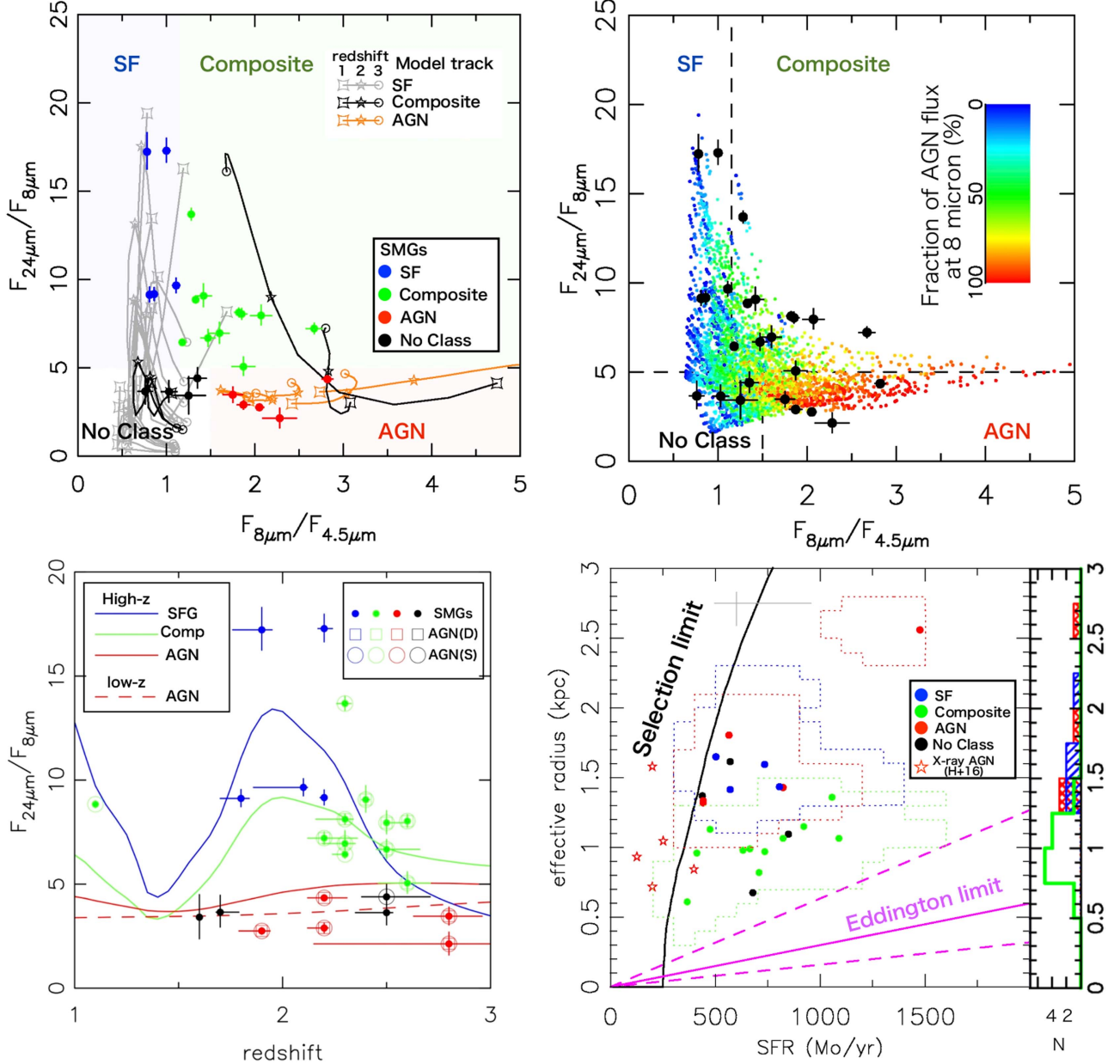


Figure 3. Relations between ALMA millimeter-wave size, SFR, and mid-IR color. Top: IRAC 4.5, 8, and MIPS 24 μm -color AGN diagnostic for $z \sim 1\text{--}3$ galaxies, based on Ivison et al. (2004). Top left: the colored shaded areas mark the diagnostic criteria of star formation (SF) dominant, composite, and AGN-dominant in mid-IR light. The solid curves are the predictions based on the SEDs in the SWIRE Template Library (Polletta et al. 2007), which is mainly composed of local star-forming galaxies, (U)LIRGs, Seyfert galaxies, and QSOs. The colored filled circles indicate the ALMA-identified SMGs. Top right: simulated mid-IR colors of mock galaxies based on empirical SED templates, with the color points showing the AGN fraction based on the mock 8 μm fluxes. The black points correspond to the ASXDF SMGs. The dashed lines show the criteria for the SF/AGN classification. Bottom left: redshift vs. 24-m/8-m colors for our sample. The solid lines indicate color evolution predictions based on empirical SED templates derived from star-forming-dominant, composite, and AGN-dominant high- z galaxy templates from Kirkpatrick et al. (2015). The dashed red line corresponds to an AGN-dominated system based on a local QSO SED template in the SWIRE template library. Open squares and circles indicate SMGs that satisfy the Donley et al. (2012) and Stern et al. (2005) IRAC AGN criteria, respectively. Bottom right: SFR vs. millimeter-wave effective radius. The colored dotted lines delimit areas where $P(\text{SFR, size}) >= 0.1 \times P_{\text{peak}}$ for each SF/AGN type. Host galaxies of X-ray-selected AGNs from Harrison et al. (2016; H+16) are marked by red stars. The size distribution of our SMGs is shown in the histogram on the right-hand side of the plot.

AGN-dominant mid-IR components are real, with a significance level of $>99\%$, according to the Kolmogorov-Smirnov test. This indicates that the composite type galaxies are characterized by more compact star-forming regions than those of the star-forming or AGN-dominant types.

We also explored the relation between size and stellar mass in our sample and found that the size differences are not a consequence of different stellar masses. Composite SMGs are the most compact of the three types, even at fixed stellar mass.

None of our ALMA-identified AzTEC SMGs are detected in the existing *XMM-Newton* X-ray maps (Ueda et al. 2008), probably because the maps are too shallow. Nevertheless, we can compare our results with the sizes derived for the host galaxies of the five high- z , X-ray-selected AGN ($L_{2-8\text{ keV}} = 10^{42.1-43.6} \text{ erg s}^{-1}$) by Harrison et al. (2016). These authors reported a size distribution for their AGN hosts similar to the SMG sizes in Simpson et al. (2015). The most X-ray luminous source in their sample ($L_{2-8\text{ keV}} = 10^{43.6} \text{ erg s}^{-1}$)

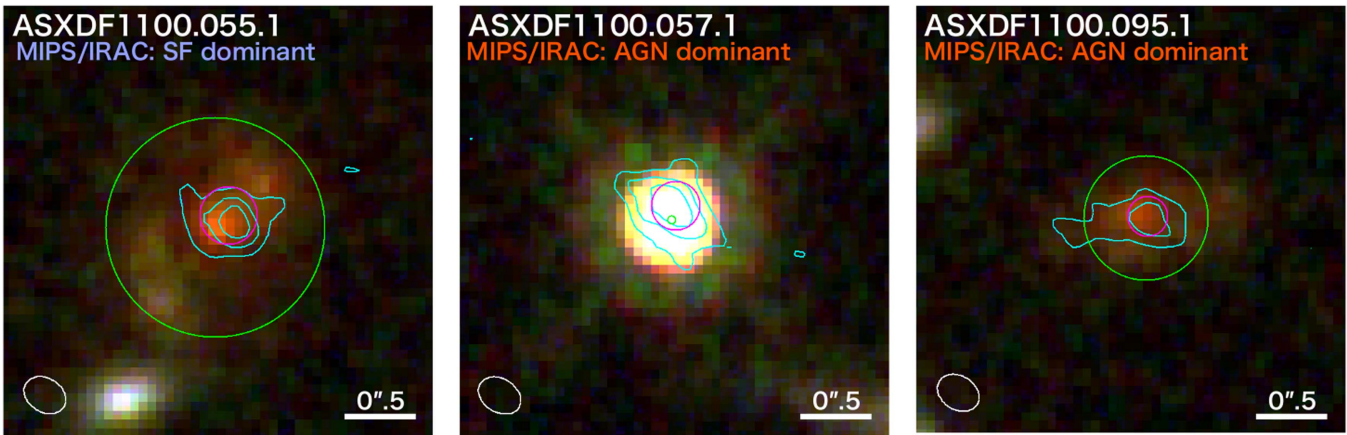


Figure 4. *HST* images with ALMA continuum contours for three of our galaxies. All images are R(1.6 μm)/G(1.2 μm)/B(0.8 μm) composites from CANDELS-UDS. The cyan contours correspond to the ALMA 1100- μm continuum ($3, 5$ and 7σ ; $1\sigma \sim 120 \mu\text{Jy beam}^{-1}$). The magenta circles indicate the circularized effective radii of ALMA 1100- μm continuum emission. The green circles correspond to the 1.6 μm continuum. The respective effective radii ($R_{\text{mir},e}$) of 6.3 ± 0.23 , $(240 \pm 1.7) \times 10^{-3}$, and 3.6 ± 0.16 kpc, for ASXDF1100.055.1, 057.1, and 095.1, after PSF deconvolution. The positions and sizes in the *HST* images are based on van der Wel et al. (2012).

has an extended size, and the remaining four ($L_{2-8 \text{ keV}} = 10^{42.1-43.4} \text{ erg s}^{-1}$) have compact sizes, which are comparable to those of our composite type here (Figure 3, bottom right).

5.3. AGN Growth During a Very Compact Star-forming Phase?

The very compact millimeter-wave sizes of the SMGs with composite mid-IR components suggest that a central supermassive black hole could be growing in a compact and coalescing star-forming phase, which is consistent with the predictions of Springel et al. (2005) for galaxy major mergers. The extended millimeter-wave sizes of the SMGs of the star-forming dominant class can be explained by a mid-stage merger as seen in, e.g., VV114 (Saito et al. 2015). Actually, ASXDF1100.055.1, with the star-forming dominant class, shows merger-like near-IR morphology (Figure 4). Instead, the extended sizes of the SMGs with the AGN-dominant class are puzzling. In line with the evolutionary scenarios of, e.g., Sanders et al. (1988), Hopkins et al. (2008), and Toft et al. (2014) where SMGs evolve into QSOs, the extended sizes may be explained by positive AGN feedback by a growing supermassive black hole in the phase of star-formation quenching, as is suggested by simulations for luminous AGN/QSOs (e.g., Ishibashi & Fabian 2012; Zubovas et al. 2013) and considered for some luminous QSOs (e.g., Carniani et al. 2016). In fact, ASXDF1100.057.1, which is an SMG of the AGN-dominant class, has a QSO-like, near-IR morphology (Figure 4). However, no significant near-IR morphological difference between AGN-host and non-AGN-host galaxies, that are not submillimeter selected, is reported (e.g., Kocevski et al. 2012). The extended submillimeter sizes in our SMGs may come from the nature of their host galaxies.

S.I. and K.I.C. acknowledge the support of the Netherlands Organization for Scientific Research (NWO) through the Top Grant Project 614.001.403. This paper makes use of the following ALMA data: ADS/JAO.ALMA#2013.1.00781.S, and ADS/JAO.ALMA#2015.1.00442.S. ALMA is a partnership of ESO (representing its member states), NSF (USA) and NINS (Japan), together with NRC (Canada), MOST and

ASIAA (Taiwan), and KASI (Republic of Korea), in cooperation with the Republic of Chile. The Joint ALMA Observatory is operated by ESO, AUI/NRAO and NAOJ.

Facilities: ALMA, Spitzer, Subaru, UKIRT, HST(STIS).

ORCID iDs

- Karina I Caputi [ID](https://orcid.org/0000-0001-8183-1460) <https://orcid.org/0000-0001-8183-1460>
- Kouji Ohta [ID](https://orcid.org/0000-0003-3844-1517) <https://orcid.org/0000-0003-3844-1517>
- R. J. Ivison [ID](https://orcid.org/0000-0001-5118-1313) <https://orcid.org/0000-0001-5118-1313>
- Laura Bisigello [ID](https://orcid.org/0000-0003-0492-4924) <https://orcid.org/0000-0003-0492-4924>
- Bunyo Hatsukade [ID](https://orcid.org/0000-0001-6469-8725) <https://orcid.org/0000-0001-6469-8725>
- Itziar Artxaga [ID](https://orcid.org/0000-0002-6590-3994) <https://orcid.org/0000-0002-6590-3994>
- Daisuke Iono [ID](https://orcid.org/0000-0002-2364-0823) <https://orcid.org/0000-0002-2364-0823>
- Takuma Izumi [ID](https://orcid.org/0000-0001-9452-0813) <https://orcid.org/0000-0001-9452-0813>
- Nobunari Kashikawa [ID](https://orcid.org/0000-0001-5493-6259) <https://orcid.org/0000-0001-5493-6259>
- Ryohei Kawabe [ID](https://orcid.org/0000-0002-8049-7525) <https://orcid.org/0000-0002-8049-7525>
- Kotaro Kohno [ID](https://orcid.org/0000-0002-4052-2394) <https://orcid.org/0000-0002-4052-2394>
- Kentaro Motohara [ID](https://orcid.org/0000-0002-0724-9146) <https://orcid.org/0000-0002-0724-9146>
- Grant W Wilson [ID](https://orcid.org/0000-0003-2705-9152) <https://orcid.org/0000-0003-2705-9152>
- Kiyoto Yabe [ID](https://orcid.org/0000-0001-6229-4858) <https://orcid.org/0000-0001-6229-4858>
- Min S Yun [ID](https://orcid.org/0000-0001-7095-7543) <https://orcid.org/0000-0001-7095-7543>

References

- Alexander, D. M., Bauer, F. E., Chapman, S. C., et al. 2005, *ApJ*, **632**, 736
- Banerji, M., Chapman, S. C., Smail, I., et al. 2011, *MNRAS*, **418**, 1071
- Biggs, A. D., & Ivison, R. J. 2008, *MNRAS*, **385**, 893
- Bisigello, L., Caputi, K. I., Grogin, N., & Koekemoer, A. 2017, *A&A*, in press (arXiv:1706.06154)
- Bothwell, M. S., Smail, I., Chapman, S. C., et al. 2013, *MNRAS*, **429**, 304
- Bradshaw, E. J., Almaini, O., Hartley, W. G., et al. 2013, *MNRAS*, **433**, 194
- Carniani, S., Marconi, A., Maiolino, R., et al. 2016, *A&A*, **591**, A28
- Chabrier, G. 2003, *PASP*, **115**, 763
- Coppin, K., Pope, A., Menéndez-Delmestre, K., et al. 2010, *ApJ*, **713**, 503
- Daddi, E., Dickinson, M., Morrison, G., et al. 2007, *ApJ*, **670**, 156
- Donley, J. L., Koekemoer, A. M., Brusa, M., et al. 2012, *ApJ*, **748**, 142
- Furusawa, H., Kosugi, G., Akiyama, M., et al. 2008, *ApJS*, **176**, 1
- Harrison, C. M., Simpson, J. M., Stanley, F., et al. 2016, *MNRAS*, **457**, L122
- Hodge, J. A., Swinbank, A. M., Simpson, J. M., et al. 2016, *ApJ*, **833**, 103
- Hopkins, P. F., Hernquist, L., Cox, T. J., & Kereš, D. 2008, *ApJS*, **175**, 356
- Ikarashi, S., Ivison, R. J., Caputi, K. I., et al. 2015, *ApJ*, **810**, 133
- Ikarashi, S., Ivison, R. J., Caputi, K. I., et al. 2017, *ApJ*, **835**, 286
- Ikarashi, S., Kohno, K., Aguirre, J. E., et al. 2011, *MNRAS*, **415**, 3081
- Ilbert, O., Arnouts, S., McCracken, H. J., et al. 2006, *A&A*, **457**, 841

- Iono, D., Yun, M. S., Artxaga, I., et al. 2016, *ApJL*, **829**, L10
 Ishibashi, W., & Fabian, A. C. 2012, *MNRAS*, **427**, 2998
 Ivison, R. J., Greve, T. R., Dunlop, J. S., et al. 2007, *MNRAS*, **380**, 199
 Ivison, R. J., Greve, T. R., Serjeant, S., et al. 2004, *ApJS*, **154**, 124
 Ivison, R. J., Papadopoulos, P. P., Smail, I., et al. 2011, *MNRAS*, **412**, 1913
 Kirkpatrick, A., Pope, A., Sajina, A., et al. 2015, *ApJ*, **814**, 9
 Kocevski, D. D., Faber, S. M., Mozena, M., et al. 2012, *ApJ*, **744**, 148
 Maiolino, R., Gallerani, S., Neri, R., et al. 2012, *MNRAS*, **425**, L66
 McLure, R. J., Pearce, H. J., Dunlop, J. S., et al. 2013, *MNRAS*, **428**, 1088
 Murray, N., Quataert, E., & Thompson, T. A. 2005, *ApJ*, **618**, 569
 Oteo, I., Zwaan, M. A., Ivison, R. J., Smail, I., & Biggs, A. D. 2017, *ApJ*, **837**, 182
 Polletta, M., Tajer, M., Maraschi, L., et al. 2007, *ApJ*, **663**, 81
 Pope, A., Bussmann, R. S., Dey, A., et al. 2008a, *ApJ*, **689**, 127
 Pope, A., Chary, R.-R., Alexander, D. M., et al. 2008b, *ApJ*, **675**, 1171
 Rosario, D. J., Santini, P., Lutz, D., et al. 2012, *A&A*, **545**, A45
 Saito, T., Iono, D., Yun, M. S., et al. 2015, *ApJ*, **803**, 60
 Sanders, D. B., Soifer, B. T., Elias, J. H., et al. 1988, *ApJ*, **325**, 74
 Serjeant, S., Negrello, M., Pearson, C., et al. 2010, *A&A*, **514**, A10
 Simpson, J. M., Smail, I., Swinbank, A. M., et al. 2015, *ApJ*, **799**, 81
 Springel, V., Di Matteo, T., & Hernquist, L. 2005, *MNRAS*, **361**, 776
 Stern, D., Eisenhardt, P., Gorjian, V., et al. 2005, *ApJ*, **631**, 163
 Swinbank, A. M., Simpson, J. M., Smail, I., et al. 2014, *MNRAS*, **438**, 1267
 Tacconi, L. J., Neri, R., Chapman, S. C., et al. 2006, *ApJ*, **640**, 228
 Toft, S., Smolčić, V., Magnelli, B., et al. 2014, *ApJ*, **782**, 68
 Ueda, Y., Watson, M. G., Stewart, I. M., et al. 2008, *ApJS*, **179**, 124
 van der Wel, A., Bell, E. F., Häussler, B., et al. 2012, *ApJS*, **203**, 24
 Wang, S. X., Brandt, W. N., Luo, B., et al. 2013, *ApJ*, **778**, 179
 Weiß, A., De Breuck, C., Marrone, D. P., et al. 2013, *ApJ*, **767**, 88
 Younger, J. D., Fazio, G. G., Wilner, D. J., et al. 2008, *ApJ*, **688**, 59
 Zubovas, K., Nayakshin, S., King, A., & Wilkinson, M. 2013, *MNRAS*, **433**, 3079